Arch. Metall. Mater. **71** (2026), 3, 993-1005

DOI: https://doi.org/10.24425/amm.2026.1990

PRZEMYSŁAW ZACKIEWICZ[1], ALEKSANDRA KOLANO-BURIAN[1*]

Fe–Co–B NANOCRYSTALLINE SOFT MAGNETIC ALLOYS WITH HIGH SATURATION INDUCTION: A REVIEW

The development of nanocrystalline soft magnetic alloys with saturation induction (B_s) approaching or exceeding 2 T remains a major materials science challenge for modern electromagnetic energy conversion systems. This review critically examines the compositional design, crystallisation kinetics, and dynamic magnetic performance of Fe–Co–B high-induction alloys, with particular emphasis on $Fe_{67}Co_{20}B_{13}$ as a model metalloid-lean composition. The interplay between chemical composition, crystallisation pathway, and nanostructural evolution is discussed as the key framework for reconciling high saturation induction with low coercivity and an adequate dynamic magnetic response. The roles of individual alloying elements are reviewed: metalloids govern glass-forming ability and crystallisation pathways, whereas transition-metal additions influence nucleation and grain growth. Special attention is given to the critical influence of saturation magnetostriction (λ_s) on alternating-current initial permeability and dynamic losses. The available data indicate that λ_s should be regarded as a primary design variable, since alternating-current permeability at 1 kHz correlates negatively with λ_s but does not correlate reliably with direct-current coercivity. Recent advances from 2024-2026 demonstrate that saturation induction above 1.9 T can be achieved in Fe-rich and Fe–Co-based nanocrystalline alloys through ultra-rapid annealing, although only within a narrow processing window. $Fe_{67}Co_{20}B_{13}$ represents a promising near-steel-loading nanocrystalline platform whose main remaining limitations are insufficient dynamic magnetic softening and limited processing window tolerance.

Keywords: Nanocrystalline alloys; Fe–Co–B; high saturation induction; ultra-rapid annealing; soft magnetic materials

1. Introduction

Soft magnetic materials are indispensable components of modern electromagnetic energy conversion systems, including traction motors, power transformers, inductors, and high-frequency power-electronic devices. As power density, switching frequency, and thermal loading continue to increase in these applications, material requirements are no longer limited to achieving low coercivity alone. Instead, the key requirement is a balanced combination of high saturation induction, low hysteresis and dynamic losses, adequate permeability, and sufficient thermal robustness under realistic operating conditions [1]. Among the currently available material classes, nanocrystalline Fe-based alloys are of particular interest because exchange coupling between nanoscale grains strongly suppresses the effective magnetocrystalline anisotropy, enabling a unique combination of soft-magnetic behaviour and compositional tunability [2,3].

The historical development of nanocrystalline soft magnetic materials has been shaped by successive efforts to overcome the intrinsic trade-off between magnetic softness and high saturation induction. FINEMET-type alloys established the archetype of controlled nanocrystallisation from an amorphous precursor, providing extremely low coercivity and very high permeability at a saturation induction of approximately 1.2-1.3 T [2,3]. Subsequent alloy generations, including NANOPERM and HITPERM, incorporated higher fractions of ferromagnetic elements and increased the attainable saturation induction to the 1.5-1.8 T range, while Fe–Co-containing systems further enhanced thermal stability and Curie temperature [3,4]. More recently, ultra-rapid annealing (URA) of Fe-rich, metalloid-lean precursors has opened a route towards HiB-NANOPERM-type materials with saturation induction approaching 1.9 T, whereas Co-containing nanocrystalline derivatives have demonstrated values comparable to, or exceeding, 2.0 T [5,6].

Within this context, $Fe_{67}Co_{20}B_{13}$ represents a particularly instructive model alloy. Its composition is deliberately positioned close to the high-induction boundary of the Fe–Co–B alloy system: the combined Fe and Co content is sufficiently high to approach the spontaneous magnetisation of Fe–Co binaries near the Slater-Pauling maximum, while the metalloid fraction is kept

[1] ŁUKASIEWICZ RESEARCH NETWORK – INSTITUTE OF NON-FERROUS METALS, 5 SOWIŃSKIEGO STR., 44-100 GLIWICE, POLAND

* Corresponding author: aleksandra.kolano-burian@imn.lukasiewicz.gov.pl

low enough to avoid excessive dilution of the magnetic sublattice. This compositional simplicity, however, also introduces a fundamental processing constraint. Unlike Nb- or P-containing nanocrystalline alloys, which benefit from improved glass-forming ability and enhanced resistance to uncontrolled grain growth, $Fe_{67}Co_{20}B_{13}$ lacks stabilising additions that would broaden the crystallisation window during conventional annealing. Consequently, the alloy offers substantial potential in terms of saturation induction, but only if the crystallisation pathway is tightly controlled [6,9-11].

A recurring limitation in the development of high-induction nanocrystalline alloys has been the tendency to prioritise grain refinement and static coercivity while underestimating the role of magnetostriction in the dynamic magnetisation process [6]. Co addition is beneficial for increasing saturation induction and improving high-temperature stability, but it also increases λ_s, which in turn intensifies magnetoelastic damping during alternating-field magnetisation [4,6]. Recent analyses have shown that alternating-current initial permeability (μ_i) at 1 kHz does not correlate reliably with direct-current coercivity (H_c), whereas a pronounced negative correlation exists between λ_s and μ_i [7,8]. These findings demonstrate that low magnetostriction is a necessary condition for suppressing excess loss and maintaining high permeability under dynamic excitation, making λ_s a primary design variable rather than a secondary material descriptor [6-9].

Preliminary work on $Fe_{67}Co_{20}B_{13}$ has shown that as-spun amorphous ribbons can be subjected to rapid heat treatment to produce ring cores with saturation induction approaching B_s = 1.99 T. Moreover, Steinmetz-type loss analysis relative to commercial N10 silicon steel indicates favourable hysteresis and dynamic-loss coefficients [11]. These observations motivate a focused review of this alloy as a high-induction nanocrystalline soft magnetic material. The aim of the present work is therefore threefold: (i) to provide a critical review of the compositional design principles governing high-induction Fe–Co–B alloys, with emphasis on the competing roles of individual alloying elements; (ii) to synthesise available data on the structure–property relationships in $Fe_{67}Co_{20}B_{13}$ and position this alloy within the broader performance landscape of high-induction soft magnetic materials; and (iii) to identify the principal barriers to further progress and outline directions for future research.

2. Performance space of high-induction soft magnetic materials

The development of high-induction soft magnetic materials has followed three main trajectories. The first is represented by classical nanocrystalline alloys such as FINEMET, which deliver exceptional softness and permeability but remain inherently limited in saturation induction. The second consists of NANOPERM- and HITPERM-type systems, where increasing the ferromagnetic-element fraction or introducing Co raises the achievable induction and operating temperature, albeit at the expense of higher magnetostriction and a deterioration in dynamic magnetic response [3,4,7]. The third trajectory is the more recent Fe-rich URA/HiB-NANOPERM route, where the deliberate reduction of non-ferromagnetic additions enables saturation induction to approach or exceed the level of Si steels, provided that crystallisation can be arrested before boride phase formation [5,6,10].

From the application perspective, NO10/N10-class thin non-oriented electrical steel constitutes the most meaningful industrial baseline, as it defines the prevailing standard for high-frequency metallic laminations in compact motors and power-electronic devices. Published NO10-class data indicate that 0.10 mm non-grain-oriented (NGO) steel attains approximately 1.10 W/kg at 1.0 T and 50 Hz, 2.84 W/kg at 1.5 T and 50 Hz, and a relative peak permeability of approximately 6200 at 1.0 T and 400 Hz [14]. More advanced thin-gauge steels substantially exceed this baseline: 10JNHF600 combines reduced high-frequency loss with a saturation induction of approximately 1.9 T, while 10JNRF attains B_{50} = 1.65 T together with 7.5 W/kg at 1.0 T and 400 Hz, constituting one of the most demanding current steel benchmarks for high-speed motor applications [12,13]. By contrast, 10JNEX900 represents the low-magnetostriction high-Si branch, combining $B_s \approx 1.8$ T with particularly attractive losses in the kilohertz frequency range [13].

Against this steel baseline, nanocrystalline materials may be grouped into three practically distinct performance classes. FINEMET still defines the softness-dominated regime, with saturation induction $B_s \approx 1.24$ T and very high permeability, but it is no longer competitive when maximum saturation induction constitutes the primary design target [2,3]. NANOPERM advanced the field into the 1.5-1.7 T range; the critical review by Suzuki attributes near-zero magnetostriction as the principal mechanism by which these alloys retain low excess loss despite only moderate coercivity [7]. NANOMET demonstrated that nanocrystalline alloys can approach 1.9 T while preserving acceptable magnetic softness and manageable magnetostriction [7]. The HiB-NANOPERM/URA family subsequently extended this range, with $Fe_{87}B_{13}$ reaching B_s = 1.92 T at H_c = 6.4 A/m, and the Co-containing alloy $(Fe_{0.8}Co_{0.2})_{87}B_{13}$ reaching B_s = 2.02 T at H_c = 9.3 A/m; the addition of 1 at.% Cu further reduced coercivity to 7 A/m while maintaining $B_s \approx 2.0$ T [5,6,7].

The significance of this progression is that the most advanced modern nanocrystalline alloys are no longer inferior to electrical steels in terms of saturation induction. The unresolved challenge is dynamic magnetic softness. The review by Suzuki [7] and the study by Huang et al. [8] converge on the same conclusion: once B_s exceeds approximately 1.7-1.8 T, further gains in induction are frequently accompanied by a substantial increase in λ_s, which intensifies domain-wall damping and excess loss. Huang et al. further demonstrated that μ_i at 1 kHz does not correlate reliably with direct-current coercivity, whereas a pronounced negative correlation exists between λ_s and μ_i [8]. Tsukahara et al. confirmed that magnetostriction is a key discriminator between alloys that exhibit high B_s and those that actually retain low core loss under alternating-field operation [9].

TABLE 1 summarises the principal performance parameters of the soft magnetic material classes discussed in this review.

TABLE 1

Representative magnetic properties and characteristic features of major classes of soft magnetic materials relevant to the present review [2-3,5-7,11-14]

Material family	B_s (T)	*Hc* (A/m)	Thickness	Loss metric	Notes
NO10-class NGO electrical steel	≈2.0	30-80	0.10 mm	P ≈ 1.10 W/kg (1.0 T, 50 Hz); P ≈ 2.84 W/kg (1.5 T, 50 Hz)	μ_i ≈ 6200 (1.0 T, 400 Hz); industrial baseline
10JNHF600 (JFE)	≈1.9	~30	0.10 mm	$W_{10/400}$ = 9.2 W/kg; $W_{10/1k}$ = 27.5 W/kg	Si-gradient high-frequency thin-gauge steel
10JNEX900 (JFE)	≈1.8	20-60	0.10 mm	$W_{10/400}$ = 5.7 W/kg; $W_{0.2T,5\ kHz}$ = 11.3 W/kg	Very low λ_s; low-noise steel benchmark
10JNRF (JFE)	≈1.65 (B_{50})	~30	0.10 mm	$W_{15/50}$ = 1.65 W/kg; $W_{10/400}$ = 7.5 W/kg	Strongest steel benchmark for high-speed motors
FINEMET ($Fe_{73.5}Cu_1Nb_3Si_{13.5}B_9$)	≈1.24	0.5-1	18-25 µm	Very low core loss	Extremely high µ; softness-dominated regime
NANOPERM ($Fe_{90}Zr_7B_3$)	1.58-1.70	3-7	18-22 µm	Low excess loss linked to near-zero λ_s	Balanced softness benchmark below steel loading
NANOMET ($Fe_{85}Si_2B_8P_4Cu_1$)	≈1.9	~5	18-22 µm	Low loss; high-B_s nanocrystalline benchmark	High B_s with balanced performance
HiB-NANOPERM $Fe_{87}B_{13}$ (URA)	1.92	6.4	18-22 µm	Core loss order-of-magnitude lower than Fe–3% Si	Cu-free URA baseline
AEROPERM ($Fe_{0.8}Co_{0.2})_{87}B_{13}$, URA	2.02	9.3	20-26 µm	High-loading benchmark; dynamic penalty from elevated λ_s	J_s > 2 T demonstrated
$(Fe_{0.8}Co_{0.2})_{86}B_{13}Cu_1$ (URA)	≈2.0	7	20-25 µm	Cu-assisted softening	Cu broadens process window
$Fe_{67}Co_{20}B_{13}$ (rapid heat treatment)	1.99	≈51	25-30 µm	Steinmetz coefficients lower than N10 [11]	Near-steel B_s; H_c above best URA; dynamic optimisation required

In the resulting hierarchy, $Fe_{67}Co_{20}B_{13}$ is appropriately described as a near-steel-loading nanocrystalline platform that is already competitive in terms of saturation induction but still requires further reduction of dynamic coercivity and improved control of the crystallisation pathway before it may be considered a fully mature alternative to the best thin-gauge electrical steels [10,11].

Fig. 1 presents the historical development of representative nanocrystalline and amorphous soft magnetic alloy families in terms of B_s as a function of introduction year or major development milestone. An upward trend in saturation induction is apparent, encompassing the successive generations from FINEMET through NANOPERM, HITPERM, NANOMET,

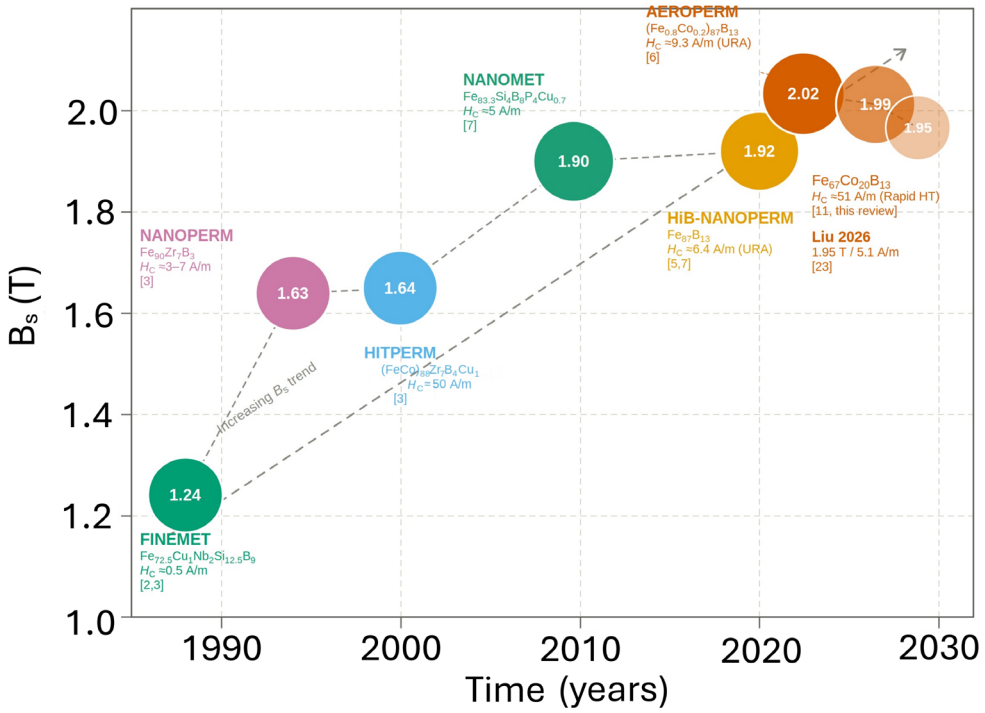

Fig. 1. Development of nanocrystalline soft magnetic alloys: principal milestones, 1988-2026. The dashed line is a guide to the eye illustrating the general upward trend in saturation induction B_s. Data from refs. [2,3,5,6,7,11,23]

HiB-NANOPERM, and AEROPERM, to the most recent rapidly annealed Fe–Co–B compositions approaching or exceeding 2 T [2,3,5,6,7,11,23]. Fig. 1 is discussed further in Section 5 in the context of recent 2024-2026 advances.

The comparative B_s vs. H_c landscape for the major material classes is illustrated in Fig. 2. This representation employs a logarithmic scale for H_c to accommodate the wide range of coercivities encountered, from below 1 A/m in classical FINEMET to several tens of A/m in Fe–Co-rich URA alloys and several hundred A/m in electrical steels. The position of $Fe_{67}Co_{20}B_{13}$ is highlighted by a filled star, indicating a composition that attains near-2 T induction but currently exhibits $H_c \approx 51$ A/m – substantially above the best URA systems [11].

3. Compositional design of Fe–Co–B high-induction alloys

3.1. General structural model

The design of high-induction Fe-based amorphous and nanocrystalline alloys is governed by the interplay between chemical composition, crystallisation kinetics, and the resulting nanostructure. A convenient framework is the generalised structural formula $(Fe,Co)_{1-x-y}M_xX_y$, where (Fe,Co) represents the ferromagnetic matrix, M denotes transition-metal additives (Nb, Zr, Cu), X denotes metalloids (B, Si, P, C), and x and y define the relative fractions of stabilising and glass-forming elements [15]. This formulation reflects the fundamental principle that nanocrystalline alloys consist of *bcc* α-(Fe,Co) nanocrystals embedded in a residual amorphous matrix, in which each compositional component fulfils a distinct functional role: the (Fe,Co) fraction determines the maximum attainable saturation induction, the metalloid fraction controls glass-forming ability and the crystallisation pathway, and the additive elements regulate nucleation and grain growth.

The prerequisite for optimal soft magnetic behaviour is the formation of a nanostructure comprising uniformly distributed α-(Fe,Co) grains with dimensions below the ferromagnetic exchange length (L_{ex}; approximately 20-40 nm), which permits averaging of local magnetocrystalline anisotropies and leads to extremely low coercivity as described by the random anisotropy model (RAM) [3]. In URA systems, composition directly determines not only the final properties but also the processing window: the separation between primary and secondary crystallisation ($\Delta T_p = T_{x2} - T_{x1}$) is strongly dependent on metalloid content and minor alloying additions [10].

Fig. 3 presents a generalised Slater-Pauling-type dependence of magnetic polarisation on the Co fraction x in binary $Fe_{1-x}Co_x$ alloys [4]. The curve exhibits a maximum near $B_s \approx 2.46$ T at $x \approx 0.27$. The position of $Fe_{67}Co_{20}B_{13}$, evaluated using the effective Co fraction within the ferromagnetic sublattice ($x_{Co,eff} \approx 0.23$), places the alloy close to the Slater-Pauling maximum, indicating that the selected Fe/Co ratio is intrinsically favourable for achieving high saturation induction. The experimentally measured $B_s = 1.99$ T [11], however, lies below the binary-alloy value, a deviation attributed primarily to dilution of the magnetic sublattice by 13 at.% B.

Fig. 4 summarises the compositional design framework for high-induction Fe–Co–B nanocrystalline alloys. The ferromagnetic component (Fe,Co) forms the backbone responsible for high B_s, with Fe acting as the primary ferromagnetic carrier and Co further increasing saturation induction and the Curie temperature while simultaneously increasing λ_s. Metalloids (B, Si, P, C) are essential for obtaining an amorphous precursor and for enabling controlled nanocrystallisation, but they dilute the magnetic sublattice and thereby reduce B_s. Transition-metal additives serve complementary roles: Cu promotes nucleation by forming pre-

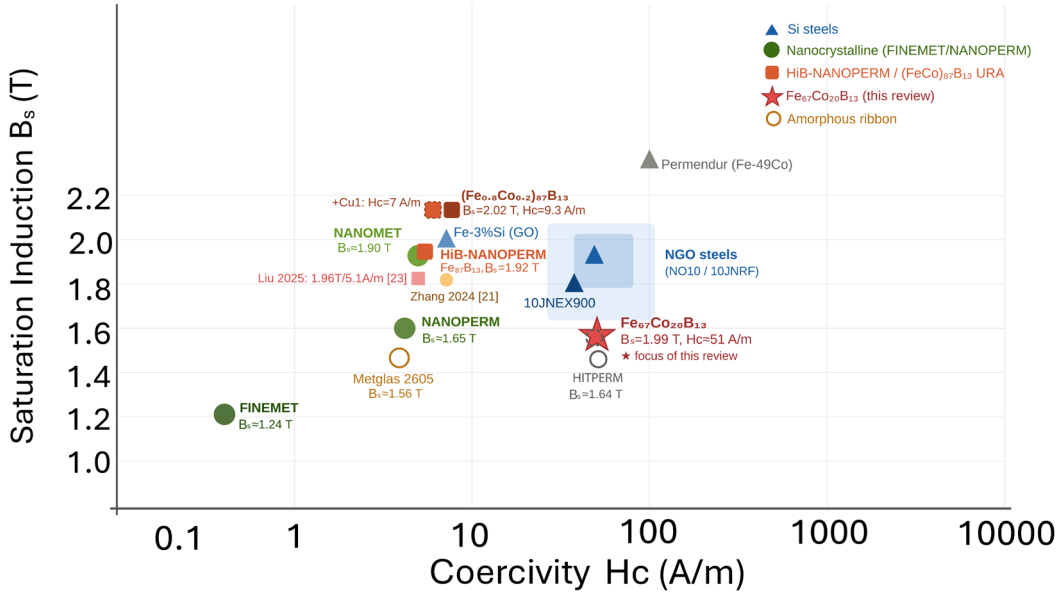

Fig. 2. Saturation induction B_s as a function of coercivity H_c for representative soft magnetic material classes. The coercive field is plotted on a logarithmic scale. Data compiled from TABLE 1 and refs. [2,3,5-7,11-14]. The position of $Fe_{67}Co_{20}B_{13}$ after rapid heat treatment is indicated by a filled star (★)

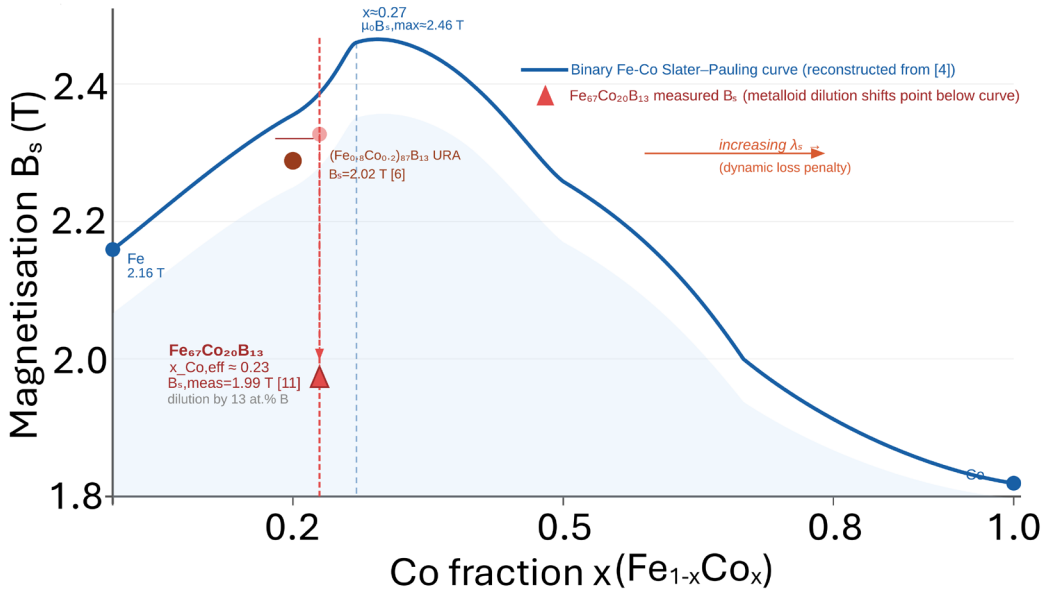

Fig. 3. Generalised Slater-Pauling curve for $Fe_{1-x}Co_x$ binary alloys. The position of $Fe_{67}Co_{20}B_{13}$ ($x_{Co,eff} \approx 0.23$) is marked; the measured $B_s = 1.99$ T [11] falls below the binary curve owing to 13 at.% B dilution. After [4]

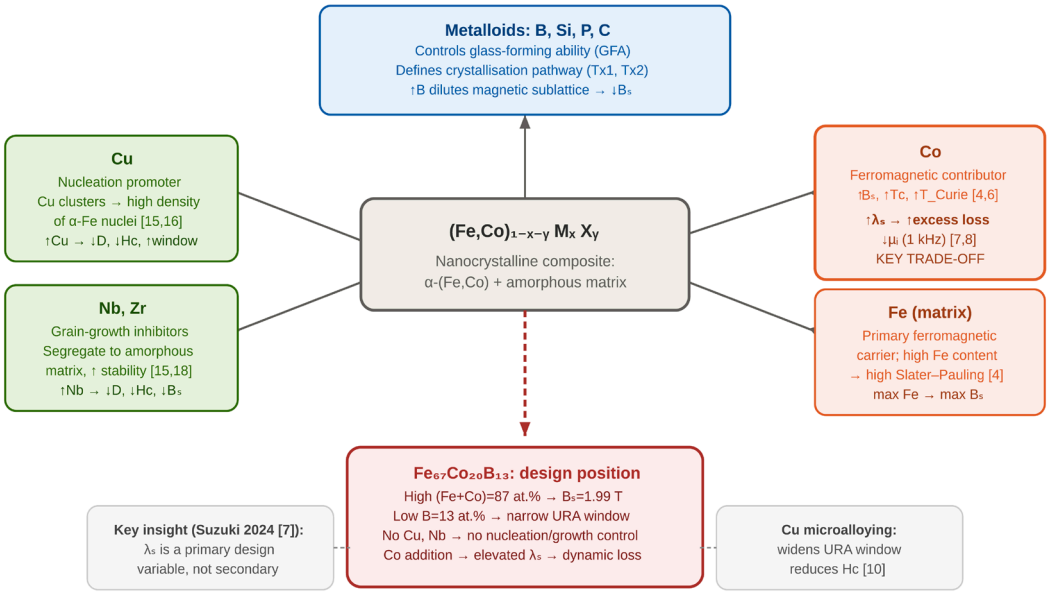

Fig. 4. Compositional design framework for high-induction Fe–Co–B nanocrystalline alloys: structural formula $(Fe,Co)_{1-x-y}M_xX_y$ and the functional roles of each alloying group. The position of $Fe_{67}Co_{20}B_{13}$ within the design space is indicated. Refs. [4,6,7,10,15-18]

crystallisation clusters, thus refining grain size and broadening the URA window; Nb and Zr act as grain-growth inhibitors by segregating to the residual amorphous matrix, though at the cost of magnetic dilution. $Fe_{67}Co_{20}B_{13}$, with Fe + Co = 87 at.% and no Cu, Nb, or Zr additions, represents an extreme high-induction design that maximises magnetic loading but exhibits high sensitivity to crystallisation kinetics and boride suppression [4,6,7,10,15-18].

3.2. Role of metalloids: B, Si, P, and C

Boron is among the most effective glass-forming elements in Fe-based amorphous alloys. In FINEMET-type systems, B improves glass-forming ability more effectively than Si, but reduces the volume fraction of ferromagnetic α-Fe precipitated during primary crystallisation [15]. Increasing B content refines the nanocrystalline grain size while simultaneously reducing the crystalline α-Fe fraction, thereby accounting for the observed reduction in B_s despite microstructural refinement. Of particular concern, Fe–B compounds such as Fe_2B and Fe_3B are magnetically detrimental, as they introduce harder secondary phases with elevated magnetocrystalline anisotropy that pin domain walls and increase H_c. Tang et al. demonstrated that in Fe-rich Fe–B alloys, increasing metalloid content reduces the separation between primary *bcc*-Fe crystallisation and secondary boride formation, directly impairing the ability to obtain a boride-free

nanocrystalline structure [10]. For $Fe_{67}Co_{20}B_{13}$, B must therefore be treated as a minimum-necessary glass former: the 13 at.% level is sufficient to enable amorphisation, but further enrichment would reduce B_s, decrease the α-(Fe,Co) volume fraction, and increase the probability of boride formation.

Fig. 5 schematically compares ΔT_p for selected Fe–B-based alloy families. Binary Fe–B compositions such as $Fe_{87}B_{13}$ and $Fe_{86}B_{14}$ possess relatively wide crystallisation intervals ($\Delta T_p \approx 100$°C and 80°C, respectively), whereas Si and P additions reduce ΔT_p to approximately 44-49°C. The incorporation of 1 at.% Cu partially restores the window to approximately 88°C by promoting a higher density of primary nuclei and improving the kinetic separation between primary nanocrystallisation and secondary boride formation. $Fe_{67}Co_{20}B_{13}$, which contains no Cu or Nb, is assigned the narrowest estimated interval ($\Delta T_p \approx 27$°C), implying that the formation of exchange-coupled α-(Fe,Co) nanocrystals must be accomplished within a very limited temperature-time range before secondary boride formation impairs magnetic softness [5,10].

Silicon improves glass-forming ability, increases thermal stability, and reduces magnetostriction. Si partitions preferentially into the α-Fe nanocrystals during annealing, while B enriches the residual amorphous matrix [15]. This partitioning is critical because the magnetostriction of the nanocrystalline alloy is highly sensitive to the Si content of the crystalline phase, and alloys with higher Si concentrations exhibit substantially reduced λ_s after nanocrystallisation – the mechanism underlying the exceptional permeability of Si-rich FINEMET [15]. Tang et al. demonstrated, however, that Si addition to $Fe_{86}B_{14}$ modifies crystallisation kinetics under rapid heating such that primary and secondary crystallisation events overlap, narrowing the effective URA window [10]. For Fe–Co–B alloys, Si therefore offers a possible pathway to reduced magnetostriction and lower dynamic losses, but would dilute the Fe–Co magnetic sublattice and may compromise the high-B_s advantage.

Phosphorus improves glass-forming ability and assists nanostructural refinement, but its effects depend strongly on alloy family and processing route. Urata et al. demonstrated that P-containing alloys can achieve high B_s and low H_c when combined with Cu: a representative $Fe_{84.8}B_8P_6Cu_{1.2}$ alloy yielded B_s = 1.78 T and H_c = 9.4 A/m, whereas the Cu-free analogue $Fe_{82}B_{10}P_8$ exhibited $H_c \approx 2460$ A/m after crystallisation [17]. Tang et al. confirmed that P, analogously to Si and C, can narrow the useful URA window in Fe-rich alloys if present in excess [10]. Carbon improves glass-forming ability at low concentrations but increases the risk of kinetic overlap between primary crystallisation and boride-forming reactions at higher contents [10]. In the context of Fe–Co–B high-induction alloys, C is therefore best regarded as a processing modifier rather than a primary performance-enhancing element.

3.3. Role of nucleation promoters and grain-growth inhibitors: Cu, Nb, and Zr

Copper acts primarily as a nucleation promoter. Hono et al. employed three-dimensional atom-probe tomography and high-resolution electron microscopy to demonstrate that Cu atoms form nanoscale clusters prior to the main crystallisation reaction, stimulating the nucleation of α-Fe nanocrystals at or near the α-Fe/amorphous interface [16]. Quantitatively, approximately 1 at.% Cu reduces the α-Fe grain size from approximately 50 nm to approximately 15 nm in FINEMET-type systems, leading to a substantial decrease in H_c and a pronounced increase in permeability [15]. Tang et al. extended this finding to URA-processed Fe–B alloys, demonstrating that 1 at.% Cu broadens the effective annealing window and restores soft magnetic behaviour even

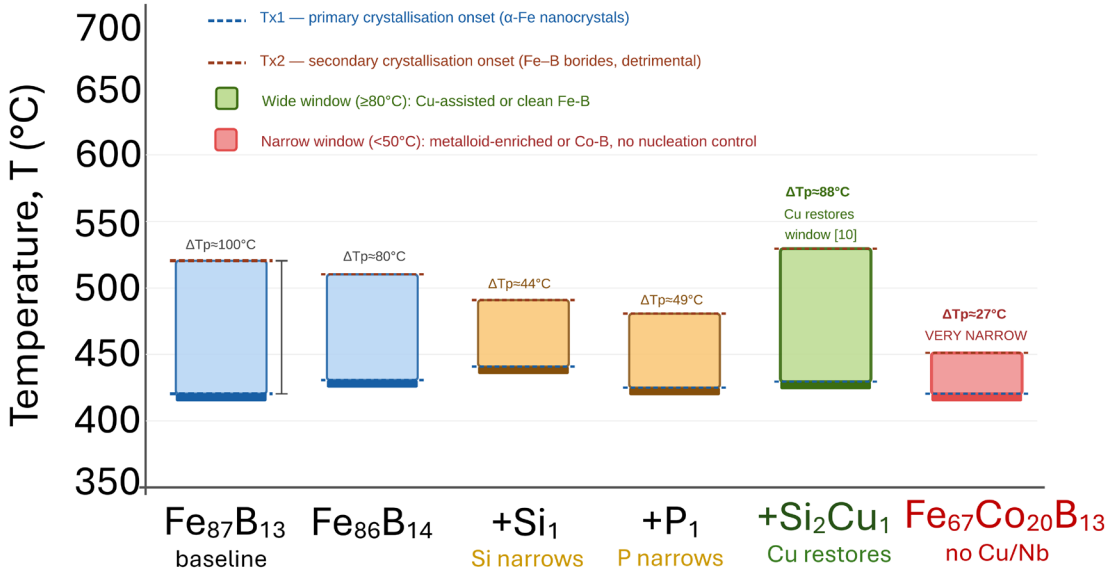

Fig. 5. Schematic URA processing window $\Delta T_p = T_{x2} - T_{x1}$ for selected Fe–B-based amorphous precursor alloys. Si and P additions narrow the window; 1 at.% Cu partially restores it. $Fe_{67}Co_{20}B_{13}$ (no Cu or Nb additions) is assigned the narrowest estimated window ($\Delta T_p \approx 27$°C). After Tang et al. [10] and Parsons et al. [5]

when metalloid additions otherwise impair URA efficiency [10]. For Fe–Co–B systems, Cu thus constitutes one of the most promising minor additions when the objective is to reduce H_c without appreciably sacrificing saturation induction, since Cu acts primarily as a process-window and nucleation-control element rather than a B_s-enhancing addition.

Niobium acts primarily as a grain-growth inhibitor. Nb is rejected from the α-Fe nanocrystals during annealing and segregates to the residual amorphous matrix, increasing its stability and viscosity and suppressing coarsening of the nanocrystalline phase [15]. The synergistic presence of Nb and Cu is particularly effective: Cu promotes dense nucleation of α-Fe, while Nb suppresses subsequent grain growth – a two-element mechanism that accounts for the exceptionally fine and homogeneous nanostructure characteristic of FINEMET [15]. Because Nb is non-ferromagnetic and has high atomic mass, additions above approximately 3 at.% yield diminishing returns: further grain refinement becomes limited while magnetic dilution increases [15]. For $Fe_{67}Co_{20}B_{13}$, Nb addition would likely improve process robustness and reduce H_c, but at the expense of reduced saturation induction.

Zirconium fulfils a role analogous to Nb but tends to exert a stronger influence on glass-forming ability. Nanocrystalline Fe–M–B alloys with M = Zr, Hf, or Nb attain favourable soft magnetic properties because the refractory-element additions segregate to the residual amorphous phase and suppress α-Fe grain growth [18]. Zr, however, has a pronounced affinity for oxygen, rendering melt-spinning and industrial processing more demanding [15]. For high-induction Fe–Co–B alloys, Zr is therefore attractive if the priority is thermal stability and low H_c, but less suitable if maximum B_s and processing simplicity are the primary objectives.

3.4. Role of cobalt: elevated B_s versus increased λ_s

Co is fundamentally distinct from Nb, Zr, Cu, B, and Si in that it contributes directly to the ferromagnetic moment and improves high-temperature magnetic behaviour. Near-equiatomic Fe–Co compositions constitute some of the highest-induction soft magnetic alloys known, but they are also susceptible to B2 ordering, embrittlement, and elevated magnetostriction [4]. In nanocrystalline Fe–B alloys, Co addition raises B_s toward 2.0 T but also substantially increases λ_s and therefore excess loss [7]. Parsons, Li, and Suzuki demonstrated that nanocrystalline $(Fe_{0.8}Co_{0.2})_{87}B_{13}$ attains B_s = 2.02 T at H_c = 9.3 A/m, and that 1 at.% Cu reduces coercivity to approximately 7 A/m while retaining $B_s \approx 2.0$ T [6].

The design-level interpretation of Co addition must account for its dual role. In comparative studies, nanocrystalline $(Fe_{0.8}Co_{0.2})_{86}B_{14}$ exhibits considerably lower μ_i than near-zero-magnetostrictive NANOPERM despite comparable direct-current coercivity, illustrating that static softness alone does not guarantee favourable dynamic magnetic properties [7]. Accordingly, the role of Co in the $Fe_{67}Co_{20}B_{13}$ system must be framed not as a straightforward attempt to maximise B_s, but as the problem of reconciling very high magnetic induction with acceptable H_c, low excess loss, and adequate permeability over the target frequency range [6-9]. Co resolves the induction limitation but simultaneously intensifies the magnetostriction and dynamic-loss constraints, establishing λ_s as a first-order design variable.

Fig. 6 illustrates the relationship between λ_s and μ_i at 1 kHz for representative Fe-based amorphous and nanocrystalline alloys, after Huang et al. [8] and Suzuki [7]. A pronounced negative correlation is observed: alloys with near-zero or low

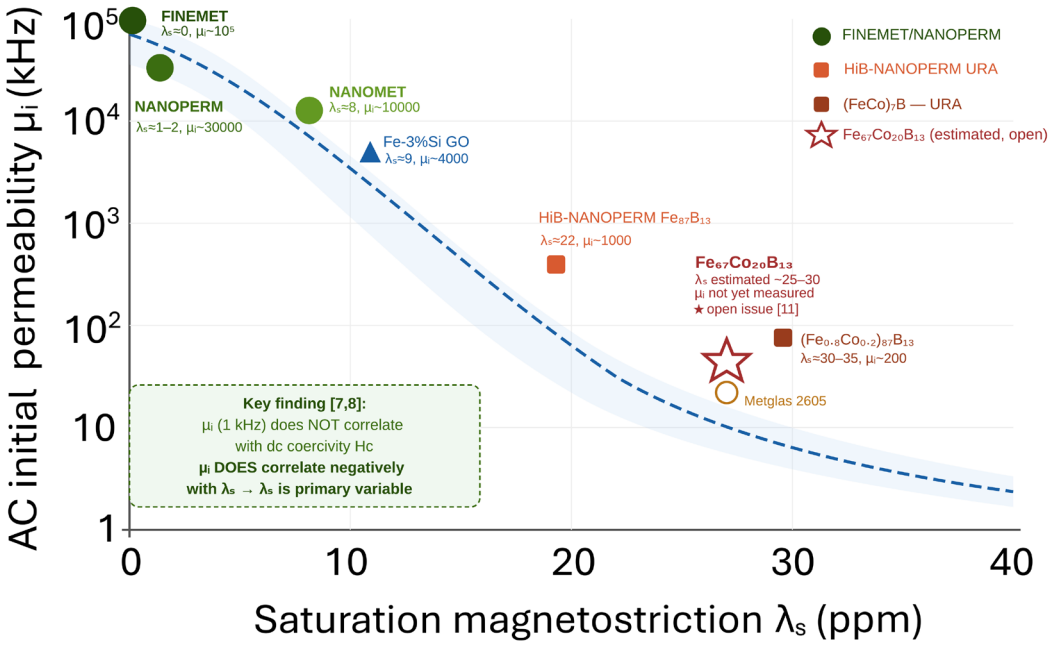

Fig. 6. Saturation magnetostriction λ_s as a primary design variable: alternating-current initial permeability μ_i (1 kHz) as a function of λ_s for representative Fe-based amorphous and nanocrystalline alloys. The position of $Fe_{67}Co_{20}B_{13}$ is estimated (open star; direct experimental values not yet reported [11]). After Huang et al. [8] and Suzuki [7]

magnetostriction, including FINEMET, NANOPERM, and NANOMET, exhibit high μ_i, whereas alloys with elevated positive magnetostriction, such as Co-rich HiB-NANOPERM, show substantially suppressed alternating-current permeability. The open star indicates the estimated position of $Fe_{67}Co_{20}B_{13}$; since direct measurements of λ_s and μ_i for this composition have not yet been reported [11], this placement is a projection based on the Co-rich chemistry and measured B_s. The figure supports the central conclusion that λ_s must be treated as an essential performance-limiting parameter in high-induction nanocrystalline alloy design.

4. $Fe_{67}Co_{20}B_{13}$ as a model high-induction system

4.1. Compositional rationale and position in the design space

$Fe_{67}Co_{20}B_{13}$ is intentionally positioned near the high-induction boundary of the Fe–Co–B design space. The combined Fe and Co content (87 at.%) is sufficiently high to approach the spontaneous magnetisation of the $Fe_{0.73}Co_{0.27}$ binary region, which lies near the Slater-Pauling maximum, while the metalloid fraction (13 at.% B) is kept low enough to avoid excessive dilution of the magnetic sublattice. The alloy lacks conventional grain-growth inhibitors (Nb, Zr) and nucleation promoters (Cu), placing it in the same design region as HiB-NANOPERM and Co-rich URA alloys [5,6,10]: high Fe+Co fraction, low metalloid content, and high sensitivity to crystallisation during thermal processing.

This compositional choice entails a direct trade-off. The high ferromagnetic-element fraction maximises the potential saturation induction; the absence of classical stabilising additions, however, removes the mechanisms that broaden the effective processing window in FINEMET- and NANOPERM-type alloys. $Fe_{67}Co_{20}B_{13}$ therefore occupies a boundary position within the design space: it offers strong potential for near-2 T performance, provided the crystallisation pathway is tightly controlled, and it inherits the dynamic-loss penalty associated with elevated λ_s in Co-rich systems [6-9,11].

4.2. Crystallisation sequence and URA processing window

Preliminary studies on $Fe_{67}Co_{20}B_{13}$ demonstrated that as-spun amorphous ribbons can be subjected to URA. In situ transmission electron microscopy (TEM) indicated a two-stage crystallisation sequence in which α-(Fe,Co) nanocrystals nucleate at the primary event ($T_{x1} \approx 420$°C), whereas continued thermal treatment promotes $(Fe,Co)_2B$ boride formation at the secondary event ($T_{x2} \approx 460$°C), which is detrimental to soft magnetic properties [11]. The onset of structural evolution and the pronounced dependence of nucleus morphology on heating rate together support the conclusion that URA is not merely beneficial for this alloy but is likely essential for obtaining a magnetically useful nanocrystalline state.

Fig. 7 schematically illustrates this two-stage crystallisation sequence and the resulting narrow URA processing window ($\Delta T_p \approx$ 30-40°C). Within this interval, exchange-coupled α-(Fe,Co) nanocrystals form within the amorphous matrix, yielding the reported $B_s \approx 1.99$ T and $H_c \approx 51$ A/m [11]. Annealing beyond T_{x2} promotes $(Fe,Co)_2B$ precipitation, which acts as a strong domain-wall pinning centre and substantially degrades soft magnetic performance. Under slow heating, the two crystallisation events may overlap; under URA, the temperature-time trajectory can pass through the critical region rapidly enough

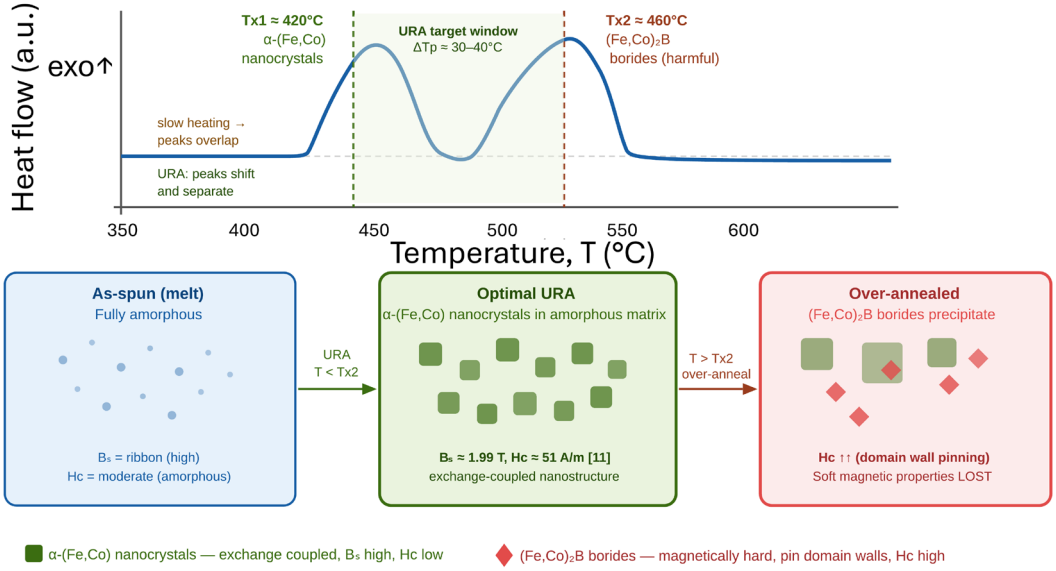

Fig. 7. Two-stage crystallisation sequence in $Fe_{67}Co_{20}B_{13}$ and the URA processing window. Schematic differential scanning calorimetry (DSC)-type heat-flow trace and corresponding microstructural states: (left) as-spun amorphous ribbon; (centre) optimal URA product with exchange-coupled α-(Fe,Co) nanocrystals; (right) over-annealed state with $(Fe,Co)_2B$ borides. Based on in situ TEM and DSC data from [11]; URA mechanism after [5,10]

to arrest the nanostructure prior to secondary boride formation.

This mechanistic picture is consistent with the broader URA literature. Tang et al. demonstrated that in Fe-rich URA alloys, increasing metalloid content narrows the useful annealing window by reducing ΔT_p, whereas 1 at.% Cu can recover the processing window by promoting a higher density of primary nuclei [10]. The binary-like character of $Fe_{67}Co_{20}B_{13}$, which lacks all classical stabilising additions, therefore places greater demands on the precision of the thermal treatment than related Cu-containing compositions such as those reported by Tang et al. [10], which attain B_s = 1.78-1.82 T with H_c = 1.4-2.8 A/m through Cu-assisted URA.

4.3. Magnetostatic and dynamic magnetic properties

Preliminary core-level measurements indicate that short annealing treatments yield ring cores with $B_s \approx 1.99$ T [11], placing $Fe_{67}Co_{20}B_{13}$ in the same induction range as the best Co-rich URA alloys reviewed in Section 2. The reported $H_c \approx 51$ A/m, however, remains substantially above the values attained by the most advanced URA Fe–B and Fe–Co–B systems, where single-digit or low double-digit coercivities have been demonstrated [5,6,10].

The relationship between direct-current coercivity and dynamic magnetic properties is a recurrent theme in high-induction Fe–Co alloys. Huang et al. demonstrated that nanocrystalline $(Fe_{0.8}Co_{0.2})_{86}B_{14}$ exhibits considerably lower μ_i than near-zero-magnetostrictive NANOPERM despite comparable direct-current coercivity, attributing this discrepancy to the elevated λ_s in the Co-rich alloy, which intensifies magnetoelastic damping under alternating-field excitation [8]. For $Fe_{67}Co_{20}B_{13}$, this implies that even if further process optimisation reduces direct-current coercivity to the level of the best URA systems, the dynamic permeability and alternating-current losses will remain strongly dependent on whether λ_s can be reduced below the critical threshold identified by Suzuki [7] and Tsukahara et al. [9]. This remains an unresolved experimental question and constitutes one of the primary open challenges in the evaluation of this alloy system.

4.4. Loss analysis and comparison with N10 silicon steel

Steinmetz-type loss decomposition for $Fe_{67}Co_{20}B_{13}$ ring cores annealed under optimised short-time conditions yields fitted hysteretic and excess-loss coefficients below those of the commercial N10 reference [11]. This finding indicates that the hysteretic contribution to total loss in the URA nanocrystalline state is governed not by static coercivity alone but by the interaction of the domain structure with the applied alternating field, and that URA processing can in principle deliver favourable loss partitioning even at near-2 T saturation induction.

Fig. 8 presents a schematic Steinmetz-based comparison of the frequency-dependent core-loss behaviour of $Fe_{67}Co_{20}B_{13}$ against the N10 reference [11,14]. Panel (a) shows total core loss as a function of frequency at constant B = 1.0 T; panel (b) presents fitted Steinmetz hysteretic (P_H) and excess-loss (P_K) coefficients normalised to N10 = 1.0. The fitted coefficients for $Fe_{67}Co_{20}B_{13}$ are approximately 0.70 and 0.65 relative to N10 for P_H and P_K, respectively, indicating a potential advantage in reducing static domain-wall pinning and dynamic excess-loss contributions. These values should, however, be interpreted as an indication of promising loss behaviour rather than a substitute for complete experimental loss maps at multiple B and frequency combinations.

The comparison must be appropriately contextualised. The fitted Steinmetz coefficients are derived from a phenomenological model and reflect hysteresis and excess-loss components under specific measurement conditions; they do not capture the full frequency dependence of total loss, direct-current-bias

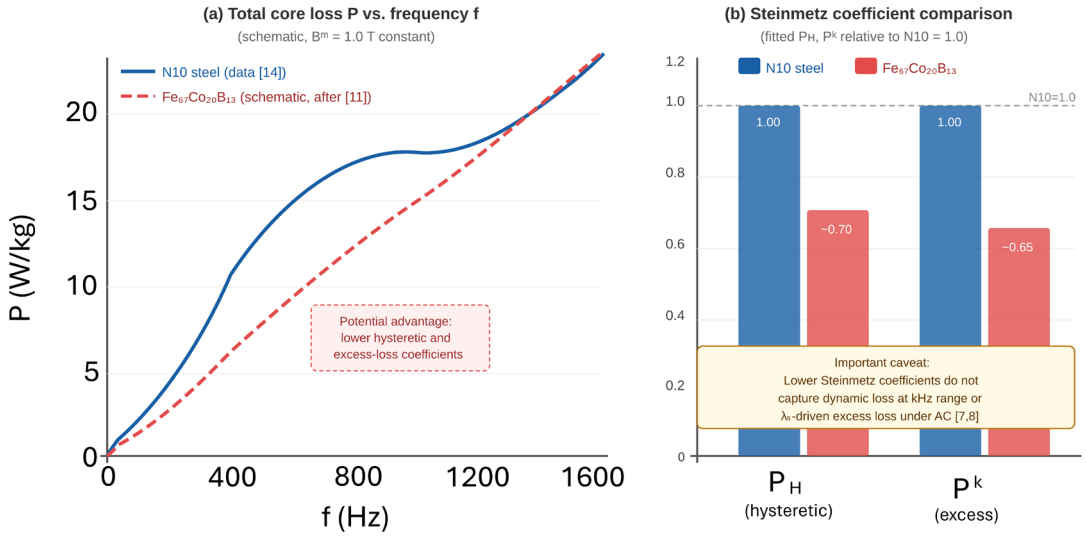

Fig. 8. Steinmetz-type loss decomposition: (a) schematic total core loss P as a function of frequency at constant B_m = 1.0 T, and (b) fitted Steinmetz loss coefficients normalised to N10 = 1.0, for $Fe_{67}Co_{20}B_{13}$ versus N10 silicon steel. Qualitative trends based on Zackiewicz [11] and Sura/Cogent NO10 datasheet [14]

behaviour, or permeability stability under realistic motor or converter excitation. Furthermore, the current $H_c \approx 51$ A/m is substantially higher than that of any commercially established nanocrystalline soft magnet, implying a considerably wider hysteresis loop under alternating-field conditions than FINEMET or optimised NANOPERM. A complete application-level loss comparison would require broadband measurements and direct-current-bias characterisation under conditions representative of the target application.

4.5. Limitations and open challenges

Three principal limitations currently constrain the performance of $Fe_{67}Co_{20}B_{13}$ as a practical high-induction soft magnet. First, the elevated H_c relative to the best URA systems reflects the narrow processing window and the sensitivity of the nanostructure to secondary $(Fe,Co)_2B$ formation. In the absence of Cu or Nb, the alloy lacks the nucleation and grain-growth control mechanisms that enable single-digit coercivities in related compositions. Second, the expected elevation of λ_s in Co-rich α-(Fe,Co) nanocrystalline alloys [7] implies a dynamic-loss penalty that is likely to persist even after further reduction of direct-current coercivity, imposing a fundamental constraint on the achievable μ_i at kilohertz-range frequencies. Third, the mechanical integrity of the ribbon and core after URA has not been systematically characterised; bendability and core winding are practical prerequisites for wound-core applications, as demonstrated by the emphasis on these properties in recent URA Fe-rich alloy studies [21,23].

Taken together, these limitations characterise $Fe_{67}Co_{20}B_{13}$ as a promising but not yet mature high-induction nanocrystalline platform. The alloy demonstrates that $B_s \approx 2$ T is achievable in a simple Fe–Co–B system without conventional grain-growth inhibitors, but also makes clear that further reduction of H_c and λ_s requires either microalloying (Cu, P additions) or more precise control of the crystallisation pathway, or both.

5. Recent advances (2024-2026) and outlook

Work published between 2024 and 2026 confirms that the development of high-induction soft magnetic materials has shifted from the classical FINEMET/NANOPERM design philosophy toward Fe-rich and Fe–Co-rich alloy systems in which the fraction of non-magnetic alloying additions is deliberately reduced. The objective is to raise B_s above 1.9 T while retaining acceptably low H_c, adequate bendability, and controlled crystallisation behaviour. Notably, modern studies no longer treat $B_s > 1.9$ T as a standalone achievement; instead, high saturation induction is evaluated in conjunction with crystallisation pathway, nanocrystal size, mechanical integrity, coercivity, and dynamic magnetic response.

Bazlov et al. investigated Fe–Co–B–Si amorphous alloys with saturation induction approaching 2.0 T and demonstrated that single-phase amorphous ribbons are obtainable for compositions with approximately 83-84 at.% metallic content, whereas an increase toward 85 at.% leads to mixed amorphous + *bcc* structures, directly confirming the central compositional trade-off: compositions most favourable for B_s are inherently the least tolerant with respect to amorphous formation [20].

Zhang et al. reported a rapidly annealed FeSiBPCu nanocrystalline alloy with $B_s \approx 1.88$ T, $H_c = 8.6$ A/m, and a bending fracture strain of approximately 1.65%, establishing that a high-Fe nanocrystalline ribbon can combine high induction, magnetic softness, and mechanical flexibility [21]. This result defines a realistic process-property target for industrially applicable Fe-rich nanocrystalline ribbons, in which the novelty resides not only in the high B_s but also in the demonstration that rapid annealing can preserve bendability while yielding a magnetically useful nanocrystalline structure.

Shi et al. provided a systematic study of the role of Cu in high-Fe-content nanocrystalline alloys, demonstrating that in Fe_{83}-based systems, optimised Cu additions of approximately 0.75-1.25 at.% enabled B_s = 1.82-1.84 T with H_c = 3.4-9.4 A/m [22]. The same investigation reported that $Fe_{85}B_8C_4Si_1P_1Cu_1$ attained B_s = 1.90 T, providing one of the clearest recent demonstrations of quantitative Cu optimisation as a design tool for high-B_s nanocrystalline alloys [22]. For $Fe_{67}Co_{20}B_{13}$, this body of work confirms that Cu constitutes primarily a process-window and nucleation-control element capable of enabling substantial reductions in H_c.

The most significant 2025 result for the Fe–Co–B field is the report by Liu et al. of FeCo-based nanocrystalline alloys reaching B_s = 1.96 T with H_c = 5.1 A/m after high-temperature short-time heat treatment [23]. This achievement addresses the central weakness of high-B_s Fe–Co systems – maintenance of low coercivity after crystallisation – and supports the hypothesis that a combination of high superheat and short annealing time can generate sufficient nucleation density while suppressing excessive grain growth and hard-phase formation. For any evaluation of $Fe_{67}Co_{20}B_{13}$, the results of Liu et al. [23] constitute the principal 2025 state-of-the-art benchmark; the gap between $H_c \approx 51$ A/m and the single-digit coercivity of [23] defines the primary target for future process optimisation.

C/P substitution in Fe–Co–B–Si amorphous alloys was demonstrated to extend the processing window by reducing T_{x1} and increasing T_{x2} relative to the base $(Fe_{0.8}Co_{0.2})_{85}B_{14}Si_1$ system [24]. This finding suggests a possible microalloying strategy for $Fe_{67}Co_{20}B_{13}$: small P or C additions may improve thermal stability and broaden the crystallisation window, but excessive content would likely reduce the maximum induction and complicate phase control. High-entropy bulk metallic glass work [25] confirms that compositional complexity can improve amorphous stability, but the elevated content of non-magnetic constituents in such alloys generally prevents competition with Fe–Co–B systems in maximum B_s.

The 2026 literature appears to be consolidating around mechanistic optimisation – particularly with respect to bendability, heat-treatment sensitivity, and the relationship between

TABLE 2

Selected advances in high-induction amorphous and nanocrystalline soft magnetic materials, 2024-2026 [20-27]

Alloy system	Processing route	Reported performance	Principal contribution	Ref.
Fe–Co–B–Si amorphous alloys	Melt spinning	B_s up to ~2.0 T	Amorphous formation limit quantified at high Fe+Co content	[20]
FeSiBPCu nanocrystalline alloy	Rapid annealing	$B_s \approx 1.88$ T; $H_c = 8.6$ A/m; bending strain 1.65%	High B_s combined with good bendability	[21]
$Fe_{85B}8C_{4Si}1P_{1Cu}1$	Optimised Cu + nanocrystallisation	$B_s = 1.90$ T	Quantified Cu–heating-rate–microstructure correlation in high-Fe alloys	[22]
FeCo-based amorphous/ nanocrystalline alloys	High-temperature short-time rapid annealing	$B_s = 1.96$ T; $H_c = 5.1$ A/m	High B_s with single-digit coercivity; key 2025 benchmark	[23]
Fe–Co–B–Si + C/P modifications	Melt spinning + controlled crystallisation	Base alloy near 2.0 T; widened processing window	C/P additions improve glass-forming ability and crystallisation separation	[24]
Co–Fe–Nb–B–P high-entropy BMG	Bulk metallic glass route	Enhanced B_s and mechanical strength	Parallel route; relevant for amorphous stability rather than maximum induction	[25]
$Fe_{83Si}4B_{10P}2Cu\_1$ nanocrystalline	Rapid annealing	Structure-softness-bendability correlation established	Mechanistic development of rapidly annealed Fe-rich alloys	[26]

nanostructure and magnetic softness – rather than establishing new saturation induction records [26,27]. This trajectory is consistent with the broader conclusion of the present review: the field has demonstrated that the attainment of saturation induction above 1.9 T is feasible, and the decisive unresolved problem is the simultaneous achievement of low λ_s and low H_c in Co-containing systems.

Fig. 9 presents a B_s–H_c performance map for high-induction soft magnetic alloys reported between 2024 and 2026, together with selected benchmark compositions. The shaded target region ($B_s > 1.95$ T and $H_c < 15$ A/m) captures the desired combination of near-2 T loading and low coercivity. Liu et al. [23] positioned the 2025 FeCo-based nanocrystalline alloy within this region at $B_s = 1.96$ T and $H_c = 5.1$ A/m, while $(Fe_{0.8}Co_{0.2})_{87}B_{13}$ also falls within the target area. $Fe_{67}Co_{20}B_{13}$ (red star) reaches $B_s \approx 1.99$ T but is displaced substantially to the right of the target region at $H_c \approx 51$ A/m, indicating that the primary challenge for this alloy is no longer the attainment of high induction but the reduction of H_c through improved control of nucleation, grain growth, and boride suppression [11].

The outlook for Fe–Co–B high-induction alloys follows from the foregoing analysis. The most promising near-term research directions are: (i) Cu microalloying of $Fe_{67}Co_{20}B_{13}$-type compositions to recover process-window robustness and reduce H_c toward the single-digit range; (ii) systematic characterisation of λ_s and its correlation with μ_i and excess loss in rapidly annealed Fe–Co–B cores; (iii) evaluation of bendability and mechanical integrity after URA as prerequisites for wound-core manufacturability; and (iv) broadband loss measurements under motor- and converter-relevant excitation conditions to establish a rigorous application-level comparison with thin-gauge electrical steels and advanced NANOPERM/NANOMET alloys. The most realistic near-term application targets are high-speed electric machines and compact power-conversion inductors in

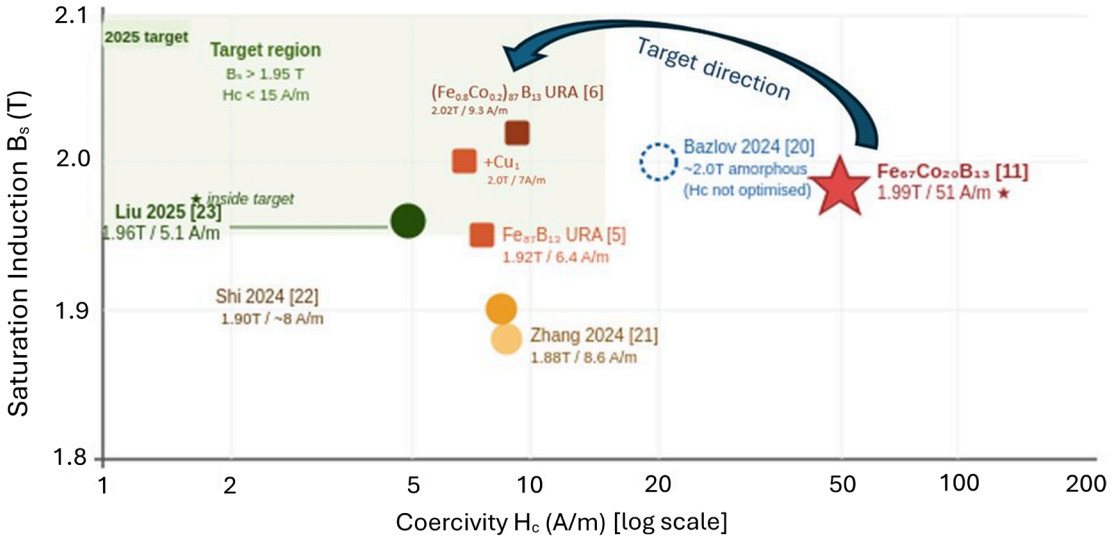

Fig. 9. B_s–H_c performance map for high-induction alloys reported in 2024-2026, with selected benchmark compositions. The shaded region indicates the target performance area ($B_s > 1.95$ T and $H_c < 15$ A/m). The coercive field is plotted on a logarithmic scale. The position of $Fe_{67}Co_{20}B_{13}$ is marked by a filled red star (★). Data from refs. [6,11,20-23]

which B_s directly limits torque density or saturation current, provided the dynamic loss constraints described above can be adequately managed.

6. Conclusions

The present review has examined the compositional design, crystallisation pathways, and dynamic magnetic performance of Fe–Co–B high-induction nanocrystalline alloys. The following principal conclusions are drawn:

(1) The transition from FINEMET-type alloys toward Fe-rich and Fe–Co-rich nanocrystalline systems represents a fundamental shift in alloy design philosophy, in which a deliberate reduction of metalloid and stabilising additions enables saturation induction approaching or exceeding 2.0 T. This compositional evolution simultaneously narrows the crystallisation processing window and increases sensitivity to uncontrolled secondary crystallisation and boride phase formation.

(2) Saturation magnetostriction (λ_s) constitutes a primary design variable governing dynamic magnetic performance. Alternating-current initial permeability μ_i at 1 kHz does not correlate reliably with direct-current coercivity but exhibits a pronounced negative correlation with λ_s [7,8]. The elevated λ_s associated with Co addition in Fe–Co–B alloys therefore imposes a fundamental constraint on achievable alternating-current permeability and excess loss, independently of the direct-current coercivity level.

(3) Individual alloying elements fulfil distinct and frequently competing roles. Metalloids (B, Si, P, C) are essential for amorphous precursor formation but dilute the magnetic sublattice and may promote secondary hard-phase formation if present in excess. Cu promotes nucleation and widens the URA processing window; Nb and Zr suppress grain growth but reduce magnetic loading. Co raises B_s and thermal stability while increasing λ_s and excess loss. High-induction alloy design must accordingly be treated as a coupled multi-variable optimisation problem.

(4) $Fe_{67}Co_{20}B_{13}$ is characterised as a model near-steel-loading system demonstrating that B_s = 1.99 T is achievable in a metalloid-lean, binary-like Fe–Co–B alloy without conventional grain-growth inhibitors [11]. The alloy exhibits favourable Steinmetz loss coefficients relative to N10 silicon steel, but its $H_c \approx 51$ A/m and the expected dynamic loss penalty from elevated λ_s indicate that substantial process optimisation is required before it may be regarded as a mature alternative to advanced thin-gauge electrical steels or to the best URA Fe–Co–B systems with single-digit coercivity.

(5) Ultra-rapid annealing is likely essential – not merely beneficial – for obtaining a magnetically useful nanocrystalline state in $Fe_{67}Co_{20}B_{13}$, because the absence of classical growth inhibitors and the two-stage [α-(Fe,Co) → $(Fe,Co)_2B$] crystallisation sequence demand precise thermal-cycle control to suppress boride formation within a narrow temperature-time window [11].

(6) Recent advances from 2024-2026 confirm that Fe–Co-based nanocrystalline alloys can reach B_s = 1.96 T with H_c = 5.1 A/m by high-temperature short-time rapid annealing [23], establishing a demanding benchmark for the further development of $Fe_{67}Co_{20}B_{13}$. The 2026 literature trend toward mechanistic optimisation of bendability, heat-treatment sensitivity, and microstructure-loss correlations [26,27] indicates that the next stage of progress will require detailed coupling of crystallisation-pathway control with dynamic loss characterisation under application-relevant conditions.

(7) The most promising near-term research directions include: Cu microalloying to improve process robustness and reduce H_c in Fe–Co–B systems; systematic λ_s characterisation and its linkage to μ_i and excess loss; evaluation of mechanical integrity after URA; and broadband loss measurements under motor- and converter-relevant excitation to enable rigorous application-level benchmarking against thin-gauge electrical steels and advanced nanocrystalline alloys.

Acknowledgements

This work was financially supported by the Polish National Centre for Research and Development [grant number TECHMATSTRATEG2/41094/4/NCBR/2019].

REFERENCES

[1] J.M. Silveyra, E. Ferrara, D.L. Huber, T.C. Monson, Soft magnetic materials for a sustainable and electrified world. Science **362** (2018). DOI: https://doi.org/10.1126/science.aao0195

[2] Y. Yoshizawa, S. Oguma, K. Yamauchi, New Fe-based soft magnetic alloys composed of ultrafine grain structure. J. Appl. Phys. **64**, 6044-6046 (1988). DOI: https://doi.org/10.1063/1.342149

[3] G. Herzer, Modern soft magnets: Amorphous and nanocrystalline materials. Acta Mater. **61**, 718-734 (2013). DOI: https://doi.org/10.1016/j.actamat.2012.10.040

[4] R.S. Sundar, S.C. Deevi, Soft magnetic FeCo alloys: Alloy development, processing, and properties. Int. Mater. Rev. **50**, 157-192 (2005). DOI: https://doi.org/10.1179/174328005X14339

[5] R. Parsons, B. Zang, K. Onodera, H. Kishimoto, T. Shoji, A. Kato, K. Suzuki, Nano-crystallisation and magnetic softening in Fe-B binary alloys induced by ultra-rapid heating. J. Phys. D Appl. Phys. **51** (2018). DOI: https://doi.org/10.1088/1361-6463/aadad6

[6] R. Parsons, Z. Li, K. Suzuki, Nanocrystalline soft magnetic materials with a saturation magnetization greater than 2 T. J. Magn. Magn. Mater. **485**, 180-186 (2019). DOI: https://doi.org/10.1016/j.jmmm.2019.04.052

[7] K. Suzuki, Recent advances in nanocrystalline soft magnetic materials: A critical review for way forward. J. Magn. Magn. Mater. **592** (2024).
DOI: https://doi.org/10.1016/j.jmmm.2023.171677

[8] H. Huang, H. Tsukahara, A. Kato, K. Ono, K. Suzuki, Effect of magnetostriction on ac initial permeability of amorphous and nanocrystalline alloys. J. Magn. Magn. Mater. **592** (2024).
DOI: https://doi.org/10.1016/j.jmmm.2024.171810

[9] H. Tsukahara, H. Imamura, C. Mitsumata, K. Suzuki, K. Ono, Role of magnetostriction on power losses in nanocrystalline soft magnets. NPG Asia Mater. **14** (2022).
DOI: https://doi.org/10.1038/s41427-022-00388-2

[10] Z. Tang, R. Parsons, K. Suzuki, Effect of metalloid additives on the effectiveness of ultra-rapid annealing in Fe-B based nanocrystalline alloys. J. Magn. Magn. Mater. **592** (2024).
DOI: https://doi.org/10.1016/j.jmmm.2024.171812

[11] P. Zackiewicz, PhD thesis, Influence of heat treatment parameters on the structure and magnetic properties of nanocrystalline Fe–Co–B alloys with Nb–P additions and elevated saturation induction for high-frequency, high-power conversion applications, Silesian University of Technology, Gliwice, Poland (2025).

[12] Gradient Si Super Core JNRF^{TM} with High Magnetic Flux Density. JFE Tech. Rep. (2024) 79-80.

[13] Y. Zaizen, T. Okubo, S. Kasai, Recent Progress of High-Silicon Electrical Steel Sheets in JFE Steel. JFE Tech. Rep. (2024) 16-22.

[14] Tata Steel / Sura, NO10-1270N Data Sheet: Thin Non-Oriented Electrical Steel. https://www.cogent-power.com [accessed: 2025].

[15] H.R. Lashgari, D. Chu, S. Xie, H. Sun, M. Ferry, S. Li, Composition dependence of the microstructure and soft magnetic properties of Fe-based amorphous/nanocrystalline alloys: A review study. J. Non-Cryst. Solids **391**, 61-82 (2014).
DOI: https://doi.org/10.1016/j.jnoncrysol.2014.03.010

[16] K. Hono, D.H. Ping, M. Ohnuma, H. Onodera, Cu clustering and Si partitioning in the early crystallization stage of an $Fe_{73.5}Si_{13.5}B_9Nb_3Cu_1$ amorphous alloy. Acta Mater. **47**, 997-1006 (1999).
DOI: https://doi.org/10.1016/s1359-6454(98)00392-9

[17] A. Urata, H. Matsumoto, S. Yoshida, A. Makino, Fe-B-P-Cu nanocrystalline soft magnetic alloys with high B_s. J. Alloys Compd. **509**, S431-S433 (2011).
DOI: https://doi.org/10.1016/j.jallcom.2010.12.104

[18] K. Suzuki, A. Makino, A. Inoue, T. Masumoto, Low core losses of nanocrystalline Fe-M-B (M = Zr, Hf, or Nb) alloys. J. Appl. Phys. **74**, 3316-3322 (1993).
DOI: https://doi.org/10.1063/1.354555

[19] A. Inoue, T. Masumoto, A. Makino, K. Suzuki, Low Core Loss of a bcc $Fe_{86}Zr_7B_6Cu_1$ Alloy with Nanoscale Grain Size. Mater. Trans. JIM **32**, 551-556 (1991).
DOI: https://doi.org/10.2320/matertrans1989.32.551

[20] A.I. Bazlov, D.A. Milkova, E.N. Zanaeva, I.V. Strochko, N.Y. Tabachkova, A. Inoue, Formation, thermal stability and soft magnetic properties of Fe-Co-B-Si amorphous alloys with ultrahigh saturation magnetic induction of 2.0 T. J. Alloys Compd. **1006** (2024).
DOI: https://doi.org/10.1016/j.jallcom.2024.176247

[21] Q. Zhang, Y. Meng, C. Zhao, C. Chang, S. Pang, S. Zhou, Rapid-annealed FeSiBPCu nanocrystalline alloy with high B_s approaching 1.9 T and good bendability. J. Mater. Res. Technol. **33**, 5204-5209 (2024).
DOI: https://doi.org/10.1016/j.jmrt.2024.10.191

[22] L. Shi, Y. Shao, J. Jia, C. Lu, K. Yao, Roles of Cu in Fe-based soft magnetic nanocrystalline alloys with high Fe content. Intermetallics **166** (2024).
DOI: https://doi.org/10.1016/j.intermet.2024.108202

[23] J. Liu, J. Cui, M. Han, W. Zhang, H. Wang, Y. Lu, T. Zhang, FeCo-based nanocrystalline alloys with excellent soft magnetic properties obtained by high-temperature short-term heat treatment. J. Mater. Res. Technol. **39**, 2157-2168 (2025).
DOI: https://doi.org/10.1016/j.jmrt.2025.09.128

[24] A.I. Bazlov, D.A. Milkova, E.N. Zanaeva, E.V. Ubyivovk, I.V. Strochko, A. Inoue, Improvement of the formation ability and soft magnetic properties of Fe-Co-B-Si amorphous alloys with ultrahigh saturation magnetization of 2.0 T by P and C additions. J. Non-Cryst. Solids **666** (2025).
DOI: https://doi.org/10.1016/j.jnoncrysol.2025.123648

[25] Y. Huo, W. Zhang, C. Zheng, Z. Zhu, Y. Li, J. Xue, L. Jiang, H. Zhang, Soft-magnetic Co-Fe-Nb-B-P high-entropy bulk metallic glasses with enhanced saturation magnetic flux density and superior strength. J. Non-Cryst. Solids **665** (2025).
DOI: https://doi.org/10.1016/j.jnoncrysol.2025.123628

[26] H. Yu, G. Zhang, S. Peng, Y. Meng, C. Chang, C. Zhao, H. Wang, Structure origin of the evolution of the soft magnetic properties and bendability for the rapidly-annealed $Fe_{83}Si_4B_{10}P_2Cu_1$ nanocrystalline alloys. J. Alloys Compd. **1064** (2026).
DOI: https://doi.org/10.1016/j.jallcom.2026.187913

[27] L. Xie, Y. Xu, Y. Zhao, F. Zhao, Z. Li, S. Shi, Z. Li, L. Hou, X. Zhang, Effect of heat treatment on microstructure and properties of FeCoBSi amorphous alloy. J. Magn. Magn. Mater. **648** (2026).
DOI: https://doi.org/10.1016/j.jmmm.2026.174033